JOURNAL OF THE AMERICAN CHEMICAL SOCIETY
Article
pubs.acs.org/JACS

Uncovering a Dynamically Formed Substrate Access Tunnel in Carbon Monoxide Dehydrogenase/Acetyl-CoA Synthase

Po-hung Wang,[†] Maurizio Bruschi,[‡] Luca De Gioia,[§] and Jochen Blumberger*,[†]

[†]Department of Physics and Astronomy, University College London, London WC1E 6BT, United Kingdom
[‡]Department of Environmental Science, and [§]Department of Biotechnologies and Biosciences, University of Milano-Bicocca, Piazza della Scienza 1, I-20126 Milano, Italy

Ⓢ *Supporting Information*

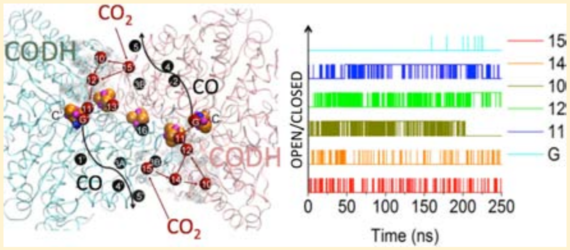

ABSTRACT: The transport of small ligands to active sites of proteins is the basis of vital processes in biology such as enzymatic catalysis and cell signaling, but also of more destructive ones including enzyme inhibition and oxidative damage. Here, we show how a diffusion-reaction model solved by means of molecular dynamics and density functional theory calculations provides novel insight into the transport of small ligands in proteins. In particular, we unravel the existence of an elusive, dynamically formed gas channel, which CO_2 takes to diffuse from the solvent to the active site (C-cluster) of the bifunctional multisubunit enzyme complex carbon monoxide dehydrogenase/acetyl-CoA synthase (CODH/ACS). Two cavities forming this channel are temporarily created by protein fluctuations and are not apparent in the X-ray structures. The ligand transport is controlled by two residues at the end of this tunnel, His113 and His116, and occurs on the same time scale on which chemical binding to the active site takes place (0.1−1 ms), resulting in an overall binding rate on the second time scale. We find that upon reduction of CO_2 to CO, the newly formed Fe-hydroxy ligand greatly strengthens the hydrogen-bond network, preventing CO from exiting the protein through the same way that CO_2 takes to enter the protein. This is the basis for directional transport of CO from the production site (C-cluster of CODH subunit) to the utilization site (A-cluster of ACS subunit). In view of these results, a general picture emerges of how large proteins guide small ligands toward their active sites.

1. INTRODUCTION

X-ray crystallography has given invaluable insight into the structural features that are built into proteins to guide the diffusion of ligands within their interior toward active sites. For a number of enzymes, it was possible to identify protein cavities that extend to tunnel-shaped structures believed to facilitate ligand transport. Examples include tryptophane synthase,[1] carbamoyl phosphate synthase,[2] hydrogenase,[3] and carbon monoxide dehydrogenase/acetyl-coenzyme A synthase (CODH/ACS).[4−6] Likewise, UV−vis and vibrational spectroscopy[7] as well as time-resolved crystallography[8] and electrochemistry[9−11] have given valuable information on the kinetics of ligand binding and unbinding at protein active sites. There are, however, several important aspects of ligand transport that are difficult to address with existing experimental methods.

Evidence is mounting that transport tunnels can form dynamically by the finite temperature fluctuations of the protein.[6,12−15] As such, they remain invisible to (static) X-ray crystallography. Moreover, while kinetic experiments typically yield an overall rate for ligand (un)binding, they usually do not give much information on whether it is the diffusion of the ligand into/out of the active site pocket or the chemical attachment/detachment of the ligand to/from the active site that determines the rate. This knowledge is highly desirable because it would open the possibility for an informed approach aimed at interfering and possibly controlling ligand transport in proteins through targeted mutation experiments. In this way, enzymes could be made more prone or tolerant to inhibition, for instance.

A promising theoretical tool that could help fill some of the gaps in our understanding of ligand transport is molecular dynamics (MD) simulation. This technique was shown to give detailed microscopic information on likely ligand transport pathways, complementing the picture obtained from crystallographic structures.[3,12−29] With computational capabilities steadily increasing, it has become possible in recent years to compute also energetic properties such as activation barriers and estimates of global free energy surfaces as well as diffusion rates.[15,23−29] These advances moved the field on, toward a more quantitative direction. However, force-field based MD methods alone are not sufficiently accurate in describing chemical binding to the active site, in particular if the active site is a transition metal cluster with a complicated electronic structure. Therefore, classical MD simulation can only give a partial picture of the true ligand binding process.

In the present work, we formulate a ligand diffusion-reaction model that overcomes this problem by describing both the

Received: April 2, 2013
Published: May 28, 2013

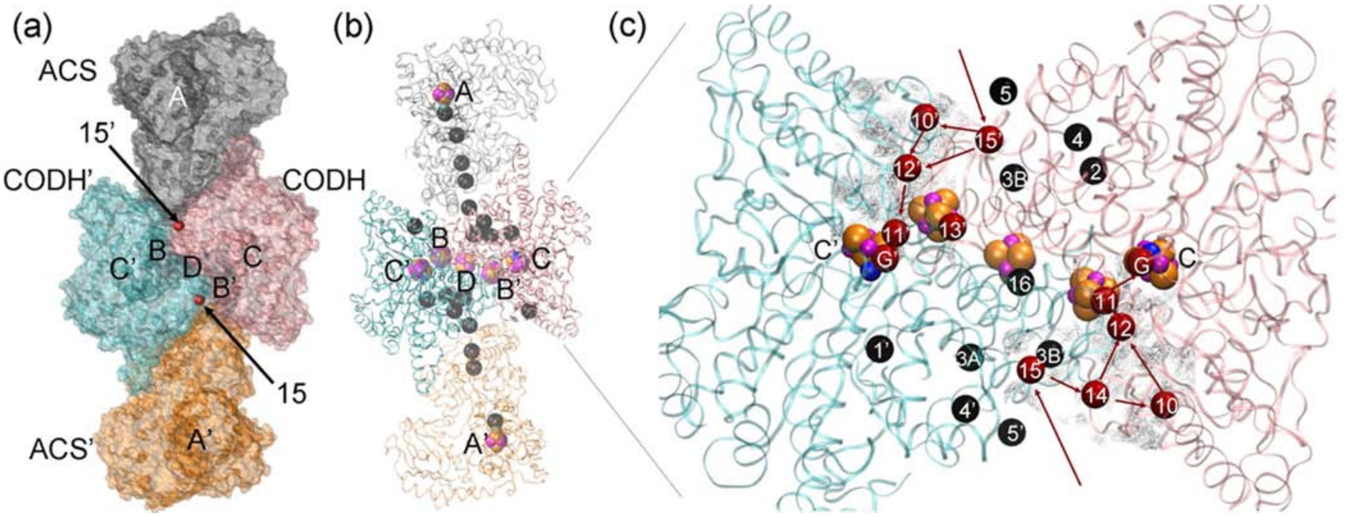

Figure 1. (a) Crystal structure of the bifunctional carbon monoxide dehydrogenase/acetyl-CoA synthase (CODH/ACS) from *Moorella thermoacetica* (Protein Data Bank ID: 2Z8Y[6]) at 2.5 Å resolution. The surfaces of the CODH′ and CODH subunits are depicted in cyan and pink, and the surfaces of the ACS′ and ACS subunits in orange and gray. The positions of the C, B, and D clusters of the CODH and the position of the A cluster of the ACS subunits are indicated as well as the entrance sites into the dynamic pathways (cavities 15, 15′). (b) Same as (a) except that the protein subunits are depicted in ribbon representation and the Xe binding sites are depicted as black spheres. (c) The two CODH subunits of panels (a) and (b) forming a dimer are shown magnified, and important cavities for ligand diffusion are indicated by spheres. Black spheres indicate the Xe-binding sites identified by X-ray crystallography[6] (cavities 1−5 and 1′−5′). They form the static pathway for ligand diffusion between C- and A-clusters. Red spheres indicate the dynamically formed pathway identified by current molecular dynamics simulations (cavities 10−15 and 10′−15′). The shape of the latter is indicated by a black mesh, and red arrows indicate a typical diffusion path of a CO_2 molecule from the solvent to the C-cluster along this path. Note that not all cavities of the static and dynamic pathway have been sampled in both CODH subunits. Only the cavities actually sampled are shown. Color code: Ni, blue; Fe, pink; S, yellow. The residues forming the cavities of the dynamic path are summarized in Table 2.

kinetics of ligand diffusion in the protein interior and the chemical binding to the active site in a unified way. Key parameters of this model can be determined by MD simulation and state-of-the-art quantum chemistry calculations. We apply this model to CO_2 transport in carbon monoxide dehydrogenase/acetyl-coenzyme A synthase (CODH/ACS), a bifunctional multisubunit enzyme that catalyzes the primary steps of carbon fixation (see refs 30, 31 for recent reviews) and that has recently attracted much interest for photoelectrochemical reduction of CO_2[32] and the design of bioinspired CO_2 reduction catalysts and sequestration technologies.[33]

CODH/ACS is comprised of four subunits, two CODH proteins and two ACS proteins; see Figure 1a. The CODH subunit houses an unusual $[NiFe_3S_4]$ cluster termed C-cluster. In the first half of the catalytic cycle, CO_2 binds to the reduced form of the C-cluster, denoted C_{red2}. In Scheme 1, we assume a dissociative mechanism, that is, dissociation of the H_2O ligand from Fe_μ followed by CO_2 binding. Upon proton-coupled 2-electron reduction of CO_2, CO is formed and released generating the oxidized form of the C-cluster, denoted C_{red1}. In the second half of the catalytic cycle, CO moves on to the A-cluster of the ACS subunit where it is reacted with coenzyme A (CoA) and a methyl group to form acetyl-CoA in a three-component reaction. The latter is an energy-rich intermediate and a precursor for the subsequent synthesis of carbohydrates.

Remarkable aspects of CODH and CODH/ACS are the structural features built into the proteins that allow for the effective transport of substrates and products. In 2001, Dobbek et al. described a continuous substrate channel in the CODH dimer from *Carboxydothermus hydrogenformans*, comprised of hydrophobic and hydrophilic regions for CO and water transport, respectively.[34] Other early experimental studies[35,36] and more recent Xe-binding X-ray crystallography studies on

Scheme 1

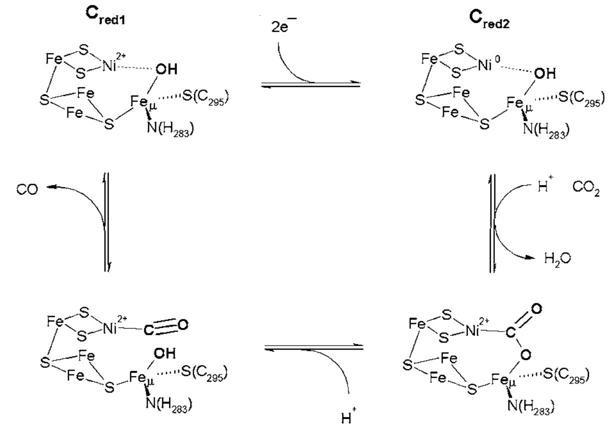

CODH/ACS[4−6] have revealed a long gas channel connecting the catalytic C-cluster of CODH with the A-cluster of ACS (see Figure 1b). Moreover, cavity calculations on CODH/ACS predicted that the two C-clusters of the two CODH subunits are interconnected by a channel.[6] Thus, a gas channel system has been identified that extends throughout almost the entire length of the enzyme complex (138 Å) connecting all four A and C-clusters.[4] Mutations of putative channel residues (A110C, A222L, A265M) resulted in decreased acetyl-CoA production rates, providing convincing evidence that CO molecules use this tunnel to travel between the two active sites, which are 70 Å apart.[20]

Yet, several important aspects of ligand transport in this enzyme complex remain puzzling. For instance, neither X-ray structures nor cavity calculations have given clues as to how CO_2 diffuses from the solvent to the C-cluster, which is buried deep inside CODH, approximately 30 Å away from the protein surface.[6] Furthermore, the CO transport "infrastructure" of the protein is nearly 100% efficient; that is, almost every CO molecule formed at the C-cluster arrives through diffusion along the tunnel system described above at the A-cluster without getting lost to the solvent.[35,36] The sequestration of CO in the protein after it is produced is of high importance because the molecule carries two reduction equivalents and is thus a valuable energy resource that cannot be wasted. Yet why does CO not merely take the same route out of the protein that CO_2 takes to get into the protein? After all, CO is smaller than CO_2, and the path that CO_2 takes to diffuse from the solvent to the C-cluster should also be accessible for diffusion of CO from the C-cluster to the solvent.

Carrying out extensive molecular dynamics simulations, we find evidence that CO_2 diffusion into the C-cluster is facilitated by a dynamical gas channel that extends orthogonal to the CO channel identified by Xe-binding X-ray studies. Solving the diffusion-reaction model, we find that diffusion through this channel and subsequent chemical binding to the C-cluster occur on similar time-scales, resulting in an overall ligand binding rate that is 3 orders of magnitude slower than diffusion or chemical binding steps alone. Our simulations also reveal that upon reduction of CO_2, the hydrogen-bond network in the active site pocket becomes so strong that it hinders CO from taking the same route out of the protein that CO_2 takes to enter the protein. The blocking of this potential leak is the basis for the directional flow of CO from the C- to the A-cluster.

2. METHODOLOGY

2.1. Diffusion-Reaction Model. We consider binding of a ligand (L) to an enzyme (E) and dissociation of the ligand-bound enzyme (B) as a diffusion-reaction process with phenomenological rate constants k_{in} and k_{out}, respectively:

$$\mathrm{E} + \mathrm{L} \underset{k_{out}}{\overset{k_{in}[\mathrm{L}]}{\rightleftharpoons}} \mathrm{B} \tag{1}$$

where [L] is the concentration of ligand in the solvent. Reaction 1 is divided into a transport process describing diffusion of L from the solvent through the protein to the active site pocket with rate constants k_{+1} and k_{-1}, respectively, and a chemical binding step with rate constants k_{+2} and k_{-2}, respectively:

$$\mathrm{E} + \mathrm{L} \underset{k_{-1}}{\overset{k_{+1}[\mathrm{L}]}{\rightleftharpoons}} \mathrm{G} \underset{k_{-2}}{\overset{k_{+2}}{\rightleftharpoons}} \mathrm{B} \tag{2}$$

In the geminate state G, the ligand carries out diffusive motion in the active site pocket but is still chemically unchanged, and in state B the ligand is chemically bound to the active site. The diffusion-reaction model eq 2 is an extension of our previously introduced approach where only diffusion (first step) was considered.[15,27,28]

To obtain the above rate constants, we carry out at first a long classical molecular dynamics simulation of ligand diffusion in the solvated enzyme. The simulation data are used to determine a probability density map of the ligand distribution within the protein, which is then coarse grained to a set of M discrete protein cavities, also denoted as states, which coincide closely with the probability maxima. Three additional states are added, one where the ligand resides in the solvent (S), one where it resides in the active site pocket (G), and one where it is chemically bound to the active site (E), giving in total $N = M + 3$ discrete states. The rate constants for the diffusive transitions between solvent and protein cavities and between the protein cavities, k_{ij}, i, j = 1 to M, S, G, are obtained from equilibrium and nonequilibrium MD simulations, and the chemical binding rates k_{+2} and k_{-2} from density functional theory (DFT) calculations (see below for details).

Assuming Markovian dynamics, the kinetics of the system is described by a master equation with the solution:

$$p_i(t) = \sum_j (e^{t\mathbf{K}})_{ij} p_j(0) \tag{3}$$

where $\mathbf{K}$ is the $N \times N$ matrix of rate constants, and p_i is the probability of occupation of state i. To obtain k_{in} and k_{out} of reaction 1, we solve eq 3 for initial conditions where the ligand population is 1 in the solvent and 0 in all other states and fit the resultant time-dependent populations of state B, $p_B(t)$, to the phenomenological rate law for reaction 1.

$$p_B(t) = \frac{k_{in}[\mathrm{L}]}{k_{in}[\mathrm{L}] + k_{out}}[1 - \exp(-(k_{in}[\mathrm{L}] + k_{out})t)] \tag{4}$$

The diffusion rate constants k_{+1} and k_{-1} are obtained similarly by propagation of a modified rate matrix that does not include the chemically bound state B (dimension $N - 1$) and fitting the resultant population $p_G(t)$ to a rate law analogous to eq 4.

An analytic relationship between k_{in} and the rate constants for diffusion and chemical binding (reaction 2) can be obtained by assuming that (i) the steady-state approximation holds for [G], that is, $d[\mathrm{G}]/dt = 0$ and that (ii) k_{-2} is negligibly small. The resultant expression takes the form:

$$k_{in}^{ss} = \frac{k_{+1}k_{+2}}{k_{-1} + k_{+2}} \tag{5}$$

where we have used the superscript ss to indicate the steady-state approximation. It should be noted that approximations (i) and (ii) are not made when propagating the master eq 3. Thus, their validity can be investigated by comparing k_{in}^{ss} with k_{in}.

2.2. MD Simulations. The simulation of CO_2 diffusion was carried out for the CODH dimer in the C_{red2} state using the coordinates from the CODH/ACS crystal structure from *Moorella thermoacetica* (Mt, Protein Data Bank (pdb) id: 2Z8Y[6]) as a starting structure. After equilibration of the solvated protein, 100 water molecules outside the solvated protein were replaced by 100 CO_2 molecules. After a short re-equilibration period, molecular dynamics simulation of the CO_2 containing aqueous protein solution was carried out for 250 ns in the NPT ensemble. The distribution of gas molecules was clustered using the Gromos clustering algorithm,[37] resulting in $N = 230$ cavities or states. The corresponding rate matrix $\mathbf{K}$ was constructed from the equilibrium simulation data according to eq 6[38] except for the slow transitions between G and the cavity connected to G (cavity 11, see Figure 1c for location within the protein) and the chemical binding step; the latter is detailed further below.

$$k_{ij} = \frac{N_{ij}^{sym}}{T_j \Sigma_{l=1}^{N} N_{lj}^{sym}} \ \forall\, j \neq i, \qquad k_{jj} = -T_j^{-1} \ \forall\, j \tag{6}$$

In eq 6, $N_{ij}^{sym} = N_{ij} + N_{ji}$ is the symmetrized number of transitions N_{ij} between cavities j and i and T_j is the average residence time of a ligand in cavity j. The rate constants for transitions from the solvent (S) to protein cavities (i), k_{iS}, were scaled by a concentration factor $V_{H_2O}^{sym}/V_{H_2O}^{\ominus}$, where $1/V_{H_2O}^{sym}$ is the concentration of a single CO_2 molecule in the solvent volume used in the simulation, and $1/V_{H_2O}^{\ominus} = [CO_2]^{\ominus}$ is the reference CO_2 concentration, $[CO_2]^{\ominus}$ = 1 mM. The scaling procedure gives the correct pseudofirst-order rate constant for solvent to protein cavity transitions at a constant CO_2 concentration. With the above choice for $[CO_2]^{\ominus}$, the overall diffusion rate constant from the solvent to the protein active site, k_{+1}, is given in units s^{-1} mM^{-1}.

A few words on the modeling of the CO_2 containing protein solution are necessary. The CO_2 concentration in the above simulations was 163 mM, which is only a factor of 5 higher than the equilibrium concentration at 1 bar gas pressure (33 mM). The high concentration was necessary to ensure sufficient sampling of protein cavities by CO_2 on the accessible time scale of current simulations. The effect of the high concentration of CO_2 on protein structure was relatively small judging from the root-mean-square deviation of the protein backbone relative to crystal structure (see Figure S2). Moreover, despite the high concentration, the population of protein cavities by CO_2 molecules is still very sparse, which means that the dynamics of CO_2 diffusion within the protein should not be significantly affected by CO_2-CO_2 interactions. However, the rate for CO_2 diffusion from the solvent into the protein does depend on the CO_2 concentration and needs to be suitably scaled as detailed above. One should also mention that in the real system a significant fraction of CO_2 exists in form of bicarbonate (HCO_3^-) at neutral pH. This equilibrium does not play a role for present calculations as long as one can assume that it is indeed CO_2, not HCO_3^-, that diffuses within the protein to the active site and that the diffusion of CO_2 is not significantly affected by the finite ionic strength of the HCO_3^- containing solution.

The rate constants for the transition 11 to G, k_{G11}, was obtained from nonequilibrium pulling simulation. CO_2 was pulled from 11 to G for a series of external forces $\vec{F}$ of constant magnitude $F = |\vec{F}|$, pointing in the direction of the vector connecting the center of mass of CO_2 and the center of the final cavity G. The time required for the transition between the two cavities was averaged over 101 trajectories with initial velocities drawn from a Boltzmann distribution at 300 K to give the mean first passage time (MFPT), $\tau_{G11}(F)$. The latter was computed for a series of forces F = 130, 140, 150, 160, 170, 180, 200 kJ mol^{-1} nm^{-1} and extrapolated to zero force using the Dudko–Hummer–Szabo (DHS) model for force-dependent kinetics:[39]

$$1/\tau_{Gi}(F) = 1/\tau_{Gi}(0)\left(1 - \frac{\nu F x^{\ddagger}}{\Delta G^{\ddagger}}\right)^{(1/\nu - 1)} e^{\Delta G^{\ddagger}\left[1-(1-((\nu F x^{\ddagger})/(\Delta G^{\ddagger})))^{1/\nu}\right]} \tag{7}$$

where $1/\tau_{G11}(0) \equiv 1/\tau_{G11} = k_{G11}$ is the rate at zero force, which is equal to the desired rate matrix element. The parameter ν was set equal to 2/3 corresponding to a linear cubic form of the energy surface. The corresponding rate constant in the identical CODH' subunit was assumed to be the same, $k_{G'11'} = k_{G11}$. The rate constant for the reverse transition from G to 11 was obtained from equilibrium simulations where a CO_2 molecule was placed, respectively, in cavities G, G′, 11, 11′, 1, and 1′. The simulations were carried out for 10 ns and repeated 20 times with different initial velocities. Assuming $k_{11'G'} = k_{11G}$, the data obtained for the two subunits were combined, and k_{11G} was computed according to eq 6. The transition times between cavities 11 and G are summarized in Table S1.

The CO escape simulations were carried out in the C_{red1} state of the enzyme using the coordinates from the CODH/ACS crystal structure from Mt (pdb id: 3I04)[40] as starting structure. For all simulations, the GROMOS96 43a1 protein force field[41] and the SPC/E model for liquid water[42] were used. Atomic charges of the C-cluster were obtained from DFT calculations and are summarized in Tables S2,S3. For CO_2 and CO, we used a 5-site[43] and 3-site model,[16] respectively. A detailed description of the molecular models and simulation protocols can be found in the Supporting Information.

2.3. DFT Calculations. DFT geometry optimizations of the C-cluster have been performed for state C_{red2} in the unbound (**1**) and CO_2-bound (**1-CO2**) form and for the transition state for CO_2 binding (**TS-1**). The calculations were carried out on the active site models shown in Figure 2, which are composed of the Fe_4NiS_4 core of the C-cluster, the side chains of the four cysteine residues coordinated to the iron and nickel atoms (Cys317, Cys355, Cys470, Cys500, Cys550), the side chain of the histidine residue coordinated to the Fe_μ atom (His283), and the side chains of residues Lys587, His113, and Asp241, which should be directly involved in the catalytic cycle. The initial coordinates were taken from the same X-ray structure that was used to initialize the MD simulations (pdb id: 2Z8Y[6]). The protein environment has been modeled by placing the molecular cluster in a polarizable continuum medium with $\varepsilon = 4$. The DFT calculations were carried out for the low-spin ground state using the BP86[44,45] exchange-correlation functional and an all-electron valence triple-ζ basis set with polarization functions on all atoms (def-TZVP). The antiferromagnetic coupling of the Fe atoms has been treated within the broken symmetry formalism. Free energy values have been obtained from the DFT self-consistent field energy by adding zero-point energy, enthalpy, and entropy contributions using standard approximations.

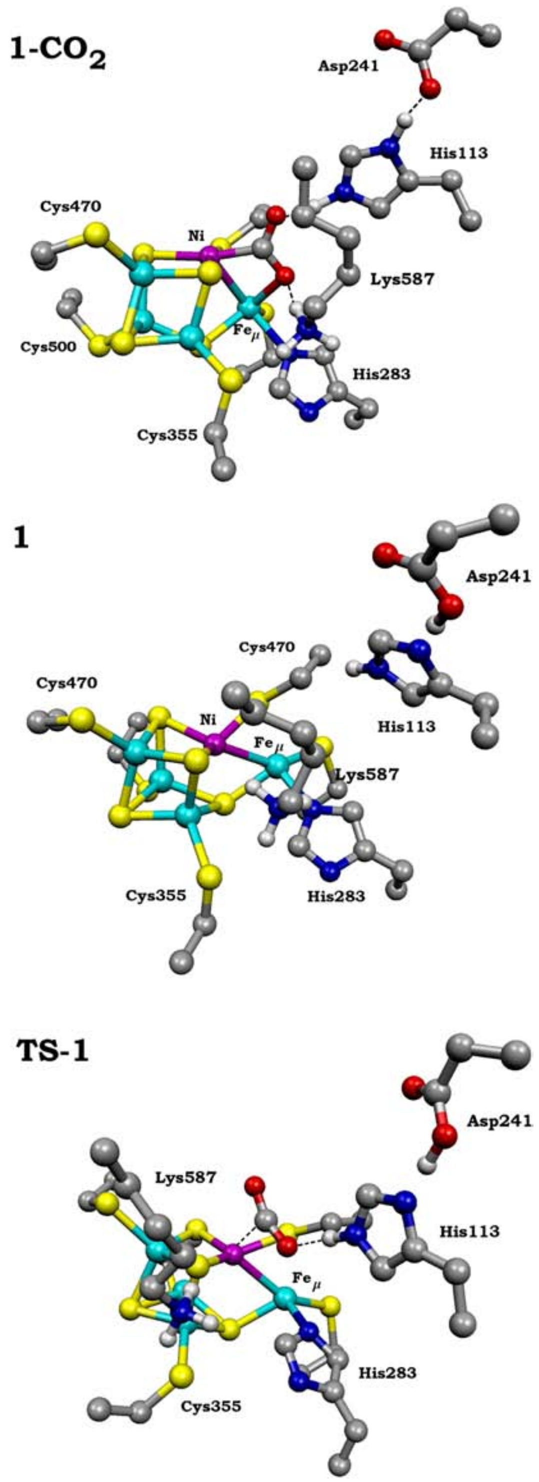

Figure 2. DFT-optimized structures of models **1-CO2**, **1**, and **TS-1**. Atom colors are cyan, violet, yellow, blue, red, gray, and white for Fe, Ni, S, N, O, C, and H, respectively. Only selected H atoms are shown. Residues are numbered according to the CODH/ACS from *Moorella thermoacetica*, pdb code 2Z8Y.

3. RESULTS

3.1. CO_2 Diffusion in Solvents. For the simulation of small molecule diffusion in proteins, it is important that the polar, hydrogen-bonding, and hydrophobic interactions between the molecule and the protein residues and solvent are well described. We have tested the CO_2 model in this respect by calculating the gas diffusion constant in a few homogeneous solvents of different polarity: water, methanol, and *n*-heptane. We find that the mean-square displacements (MSD) increase linearly with time indicative of Einstein diffusion (see Figure S1). The corresponding diffusion coefficients are summarized in Table 1. We find that the experimental trend, an increase in diffusivity with decreasing polarity, is well reproduced. Moreover, the calculated values are reasonably close to the experimental ones. For water and *n*-heptane, the diffusion coefficient is overestimated by 24% and 15%, respectively, whereas for methanol it is slightly underestimated by 2%. These results indicate that the CO_2 model is suitable for the calculation of diffusion rates in protein. The CO model gives similarly good agreement with experiment as reported previously.[27]

Table 1. Diffusion Constants for CO_2 in Various Solvents in Units of 10^{-5} cm^2 s^{-1}

solvent	calculated	experiment
water	2.5 ± 0.2	1.91[a]
methanol	5.0 ± 0.5	5.13[b]
n-heptane	7.1 ± 1.0	6.03[c]

[a] Reference 54. [b] Reference 55. [c] Reference 56.

3.2. Discovery of a Dynamically Formed Channel in the CODH Dimer. We find that many CO_2 molecules sample the surface cavities of the CODH dimer, but only a few of them can deeply penetrate the protein within a total simulation time of 250 ns. The fraction of molecules inside the protein converges after about 50 ns to 38%. The corresponding concentration of CO_2 in the protein is a factor of 2.7 higher than in the solvent, indicating a slight preference for molecules to occupy the protein. However, as mentioned before, most of the molecules are in the cavities at the protein surface. We note that the presence of molecules does not significantly impact on protein structure. The RMSD reaches a plateau value of 1.8 Å after about 50 ns simulation time (Figure S2(b)), a value similar to the one obtained for the protein system without gas (1.9 Å, Figure S2(a)). Only after about 150 ns does the RMSD increase to 2.3 Å.

The cavities obtained by coarse graining the probability density of CO_2 inside the CODH dimer are depicted in Figure 1c by black and red spheres. Not all cavities have been sampled in both CODH subunits during the MD simulation, but because they are related by symmetry, we can combine the results obtained for each monomer. We use a combination of numbers and letters to denote the cavities. The black cavities were found by Xe-binding X-ray crystallography[6] and in the present MD simulations *and* are labeled as in ref 6 (1, 2, 3A, 3B, 4, 5). Omitting cavities 6−9 that are located in the ACS subunit,[6] the additional cavities in the CODH subunit found by MD simulation are shown in red and are labeled from 10 to 15. The cavity at the active site pocket is labeled G (for geminate state).

The cavities depicted in black form a channel that leads from the CODH/ACS interface at cavity 5 to cavity 1. The latter is 10 Å away from the Fe_μ atom of the C-cluster. We denote this pathway as "static" because the cavities that form this pathway (1, 2, 3A, 3B, 4, 5) have been identified in Xe-binding X-ray studies.[6] However, no transition between cavity 1 and the active site cavity G was observed. Remarkably, the simulations reveal an as yet unidentified tunnel depicted in Figure 1c by red spheres. CO_2 enters this pathway typically via cavity 15 and can readily move on to cavity 11. The final passage from 11 to G is narrowed by the presence of His113 and His116. As a consequence, only one such transition through this motif is observed in the present 250 ns MD simulation. We denote the route connecting 15 with G a "dynamic path" because it is formed dynamically and is only observed in MD simulations but not in available crystal structures. We should note that cavity 10 was in fact found in Xe-binding studies and is thus not dynamically formed. However, as it is part of the dynamic path, we have colored it in red. The residues lining the dynamic path are summarized in Table 2.

Table 2. Residues Forming the Cavities of the Dynamic Path within the CODH Dimer

cavity index[a]	residue[b]
11	Ala112, His113, His116, His283, Asn284
12	His119, Leu286, Ala375, Tyr388, Gln389, Thr390
13	Ala111, Cys114, Glu115, Asn118, His209, Glu214
14	Lys178, Asp376, Tyr388, Gln389
15	Lys178, Gly179, Glu180, Asn202, Phe206

[a] See Figure 1c. [b] Residue numbers of CODH/ACS from *Moorella thermoacetica*, pdb code 2Z8Y.[6]

The opening and closing of the protein cavities that form the dynamic tunnel was investigated in more detail. A cavity is defined to be "open" if a spherical particle with probe radius 1.6 Å fits in the cavity defined by the van der Waals radii of the surrounding atoms, and defined to be "closed" otherwise. The probe radius was chosen so that all cavities that bind Xe in the crystal structure are open after Xe is removed (see Figure 3a, squares). The average obtained from the MD trajectory is between 75% and 100% (○), which means that the cavities of the static path remain open most of the time. An exception is cavity 5 at the protein surface, which becomes filled with solvent molecules during the MD and is thus defined as closed for most of the time. However, we found that water molecules in that cavity are very mobile and exchange fast with CO_2 or bulk solvent molecules.

The picture is strikingly different for the cavities of the dynamic path. In the crystal structure, the cavities at the protein surface (15, 14, 10) are open (panel (b), squares), but, importantly, the two cavities inside the protein, 12 and 11, are closed. We find that thermal protein motion leads to a temporary expansion of the latter two cavities, resulting in an open state at 40% and 70% of the time. These open states facilitate transport of CO_2 to the C-cluster. The time series of the opening/closing events are shown in panels (c) and (d) for static and dynamic pathways, respectively. The transitions are in general very rapid, and only the cavities of the static path remain open for a prolonged period of time. Notably, the active site cavity G is closed most of the time and opens only on a few occasions.

3.3. Structure of C-Cluster. The DFT-optimized structures of the C-cluster in state C_{red2} in the unbound (**1**) and CO_2-bound (**1-CO2**) forms are shown in Figure 2 (for details

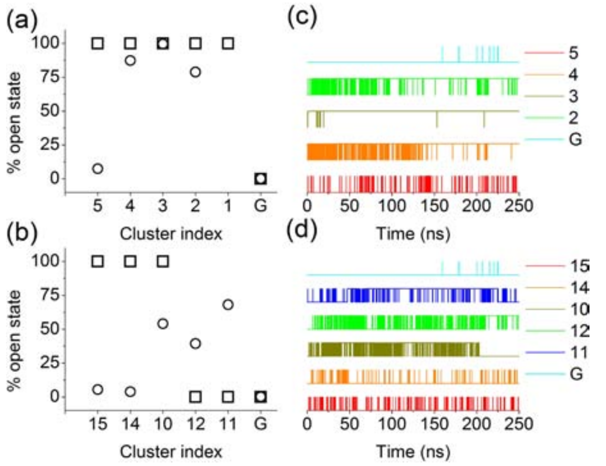

Figure 3. Dynamics of tunnel formation. On the left-hand side the percentage of the simulation time is shown in which the cavities of the static (a) and dynamic (b) paths are in the "open" state (○). The state in the crystal structure is also shown (squares, 100% = open, 0% = closed). The time series used to obtain the averages in (a) and (b) are shown in panels (c) and (d). "Up" means open, and "down" means closed. The probe radius was set to 1.6 Å, and the time resolution was 50 ps.

of calculations, see section 2.3 and Supporting Information). In **1-CO2**, the C atom of CO_2 is bound to Ni, completing its square planar coordination, and one O atom is bound to Fe$_\mu$, as found in the crystallographic structure of CODH from *Carboxidothermus Hydrogenoformans* (CODHCh; pdb code 3B52).[46] The optimized geometry of **1-CO2** fits fairly well the corresponding X-ray structure of CODHCh, as the RMSD of the $[Fe_4NiS_4(C_2H_5S)_4(C_5N_2H_8)(CO_2)]$ cluster is 0.36 Å with respect to the X-ray structure. In particular, the Fe$_\mu$−Ni distance (2.78 Å) is in very good agreement with the X-ray structure of CODHCh (2.8 Å), while the average Fe−Fe distance is about 0.06 Å larger. The C atom of CO_2 is coordinated to the Ni atom at a distance of 1.87 Å, a value smaller than that observed in the X-ray structure (1.96 Å), but very close to the corresponding value in the crystallographic structure refined by Fontecilla-Camps et al. (1.86 Å).[47] On the other hand, the Fe$_\mu$−O(CO) distance is equal to 2.23 Å, a value significantly larger than in the X-ray structure (2.05 Å). In this respect, it is worth noting that in a larger model, also including a water molecule H-bonded to the coordinated O atom, the Fe$_\mu$−O(CO) distance decreases to 2.15 Å without significantly affecting other geometrical parameters. The CO_2 molecule in **1-CO2** is one-electron reduced, as indicated by the NBO charge equal to −1.05. This form is probably stabilized by the formation of H-bonds between the two O atoms of CO_2 and the protonated His283 and Lys563 residues. The atomic spin density on Ni is negligible, indicating that it is diamagnetic, as observed in L-edge and K-edge X-ray absorption studies.[48,49]

In the CO_2-unbound model **1**, the Ni atom should be formally 3-fold coordinated by Cys526 and two sulphide ions. However, we found that in the optimized structure of **1**, the Ni atom moved closer to Fe$_\mu$ and assumed a flattened tetrahedral coordination. Also, in this case, the Ni atom can be described as diamagnetic because the calculated atomic spin density is very small (less than 0.15). The transition state (TS) along the reaction coordinate corresponding to CO_2 binding (**TS-1**), characterized as explained in the Supporting Information, is also reported in Figure 2. In the TS, the Ni−C(O2) and Fe$_\mu$−O(CO) distances are equal to 2.95 and 4.33 Å, respectively. In addition, the CO_2 molecule is slightly activated as the O−C−O angle is equal to about 153°. The energetics for the chemical binding of CO_2 is discussed in the following section.

3.4. CO_2 Binding Kinetics. The diffusive transitions of CO_2 between solvent and protein cavities and between protein cavities are rather fast, on the time scale of $\tau_{ij} = 1/k_{ij} = 0.1 - 1$ ns. Hence, they are well sampled on the MD time scale. An exception is the slow final transition from cavity 11 to the active site cavity G that was observed only once in the unbiased MD simulations. We have used constant force pulling to obtain an improved estimate for the rate constant for this transition (see section 2 for details). The mean first passage time (MFPT) for transition from cavity 11 to G as a function of the pulling force is shown in Figure 4a. The data fit the Dudko−Hummer−Szabo model[39] for force-dependent kinetics well (eq 7) with a correlation coefficient of 0.997. The fit at zero force gives an MFPT of τ_{G11} = 410 ns. The MD estimates of the transition rates are then inserted into the master eq 3, which is solved to obtain the time-dependent population of the active site cavity G, depicted in Figure 4b. We observe a monoexponential increase in the population, fitting well the phenomenological kinetic equation of the form of eq 4 with a correlation coefficient of 0.98. From the fit we extract the phenomenological rates for diffusion from the solvent to G, $k_{+1} = 4.8 \times 10^3$ s^{-1} mM^{-1}, and for the reverse direction, $k_{-1} = 1.5 \times 10^7$ s^{-1} (Table 3).

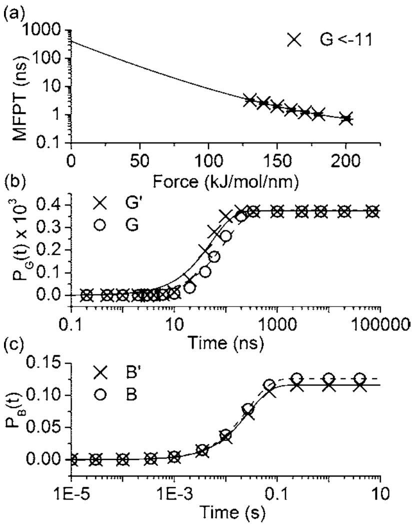

Figure 4. (a) Mean first passage time (MFPT) for transition of CO_2 molecules between cavities of CODH as obtained from constant-force pulling simulation. The MFPT is shown as a function of pulling force for the transition G←11. See Figure 1c for the location of the cavities within the protein. Statistical error bars for each pulling simulation are indicated, but may be smaller than the symbol size. Fits to eq 7 are shown in solid lines. Populations of the geminate state (G) and the ligand bound state (B) are shown as a function of time in panels (b) and (c), respectively. Data points are obtained by solving the master equation (eq 3) for the population of state G or B in the two subunits CODH and CODH′, respectively. Fits to the phenomenological first-order equation (eq 4) are shown as solid and dotted lines, respectively. Rates obtained from the fits are summarized in Table 3.

The energetics of chemical binding of CO_2 to the C-cluster was investigated by DFT calculations on a cluster model of the C-cluster (see section 2 and Supporting Information for

Table 3. Rate Constants for CO_2 Diffusion (k_{+1}, k_{-1}) and Chemical Bond Formation to the C-Cluster of the CODH Dimer (k_{+2}, k_{-2}), and the Overall Ligand Binding Rate Constants (k_{in}, k_{out}) at 300 K[a]

k_{in} (s^{-1} mM^{-1})[b]	4.4 ± 0.7
k_{in}^{ss} (s^{-1} mM^{-1})[c]	4.2
k_{out} (s^{-1})[b]	32 ± 6.4
k_{+1} (10^3 s^{-1} mM^{-1})[d]	4.8 ± 0.8
k_{-1} (10^7 s^{-1})[d]	1.5 ± 0.3
k_{+2} (10^4 s^{-1})[e]	1.3
k_{-2} (s^{-1})[f]	32

[a] Values averaged over the two CODH monomers. Values for each separate monomer are given in Table S1. Error bars are obtained from block averages of the MD trajectory using a block length of 50 ns. [b] From fit of $p_B(t)$ to eq 4; see Figure 4c. [c] Equation 5. [d] From fit of $p_G(t)$ to expression similar to eq 4; see Figure 4b. [e] From the DFT activation free energy using transition state theory. [f] Obtained as explained in section 3.4.

details). The free energy barrier obtained is 11.9 kcal/mol, which we have converted into the rate for chemical binding using transition state theory (k_{+2}, Table 3). The rate matrix constructed above for diffusive transitions is modified to include the chemical binding step and is solved to obtain the time-dependent populations of the chemically bound state B. We have found that the BP86 functional overestimates the binding free energy of CO_2 to the C-cluster and hence underestimates k_{-2}. Using experimental data, an improved estimate for k_{-2} was obtained as follows. The latter was chosen so as to obtain values for k_{in} and k_{out} that reproduce the experimental Michaelis–Menten constant, $K_M = (k_{out} + k_{cat})/k_{in} = 7.4$ mM,[50] for the experimental k_{cat} (1.3 s^{-1} [50]).

The time-dependent populations obtained with the adjusted value for k_{-2} are shown in Figure 4c. From the fit to eq 4, we obtain $k_{in} = 4.4$ s^{-1} mM^{-1} and $k_{out} = 32$ s^{-1}. All rate constants obtained are summarized in Table 3, where k_{+1}, k_{-1}, k_{+2}, and k_{in} are solely obtained from MD and QM calculations, and k_{-2} and k_{out} by combining the calculations with the experimental values for K_M and k_{cat}. We find that the steady state expression eq 5 gives $k_{in}^{ss} = 4.2$ s^{-1} mM^{-1}, which is equal to k_{in} within the statistical error margins. As k_{-2} is indeed small, this suggests that the steady-state approximation for state G is an excellent approximation.

3.5. Guided Escape of CO. After CO_2 is bound to the C-cluster in the C_{red2} state of the enzyme, it undergoes two proton-coupled electron transfer reactions resulting in the formation of the C_{red1} state, where CO is bound to the Ni atom and a OH group (derived from an oxygen atom of CO_2) to the Fe_μ atom. To probe the mobility of the CO ligand in the C_{red1} state, we placed one molecule in each of the two active site cavities (G) and initiated 20 independent trajectories of length 20 ns, giving in total 40 CO trajectories. We found that in 13 trajectories a CO molecule transits from G to cavity 1 and moves along the static path toward cavity 5 at the interface where ACS binds. Intriguingly, none of the CO molecules reach cavity 11, that is, escape the protein via the dynamic pathway. This is consistent with experimental evidence suggesting that CO transport from CODH to ACS occurs via the static pathway.[6]

Yet, why does CO not simply exit the active site through the dynamically formed tunnel that CO_2 takes to enter the active site? After all, the simulations in section 3.2 have shown that CO_2 can spontaneously leave the active site along either the dynamic or the static tunnels in the C_{red2} state of the enzyme; see Figure 5a. To explain this result, we note that in the C_{red2} state there are three water molecules between the active site and the first cavity of the dynamic path (cavity 11). Together with Lys587, His113, and His116, they form a loose hydrogen-bond network that can be easily crossed by CO_2 ("dynamic path" in Figure 5a). Upon CO_2 reduction and formation of the Fe-hydroxy ligand coordinated to Fe_μ, this ligand forms a strong hydrogen bond to a neighboring water molecule that in turn forms hydrogen bonds with another water molecule and with His113 (see Figure 5b). The strengthening of the local hydrogen-bond network in the active site induced by the Fe-hydroxy ligand prevents CO from diffusing out along the dynamic path. The only feasible exit from the active site is to diffuse to cavity 1 and along the static path to the interface where ACS binds.

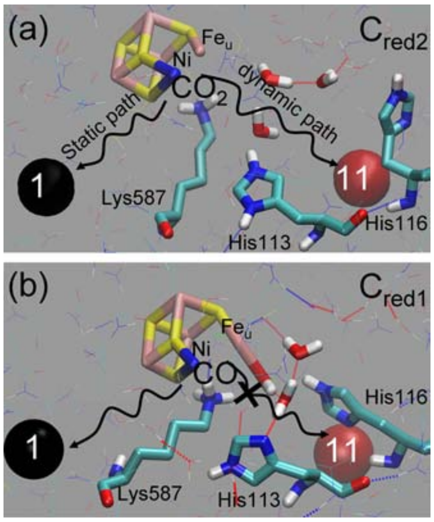

Figure 5. Hydrogen-bond network in the active site pocket (C-cluster) of CODH (a) in the C_{red2} and (b) in the C_{red1} states. The snapshots are taken from equilibrium molecular dynamics runs of the CODH dimer with a CO_2 and a CO molecule occupying the active site pocket (cavity G) in states C_{red2} and C_{red1}, respectively. Hydrogen bonds are shown as dashed lines. The cavities of the static and dynamic diffusion paths that are closest to the active site, 1 and 11, respectively, are indicated by spheres. Note that in state C_{red1}, the Fe_μ atom is coordinated by a hydroxo group (derived from an oxygen atom of CO_2 and a proton from His113). This group strengthens the hydrogen-bond network so that CO can escape the active site pocket only via the static path. Color code: Ni, blue; Fe, pink; S, yellow; O, red; N, blue; C, cyan; H, white.

4. DISCUSSION

We have carried out long MD simulation of the CODH dimer subunit of CODH/ACS and discovered a dynamical pathway for CO_2 transport that runs orthogonal to the experimentally identified static pathway. Our simulations give a theoretical confirmation of speculations of Doukov et al. that the CO_2 pathway is dynamic in nature and thus not evident from Xe-binding studies.[6] On the other hand, our results are not supportive of the hypothesis that CO_2 preferentially diffuses along the static path toward the CODH active site,[51] a proposal that was considered as unlikely[6] because it meant that CO and CO_2 would use the same gas channel but in opposite directions. To substantiate this view, we carried out additional calculations to estimate the rate for transitions from the final cavity of the static pathway, cavity 1, into G using constant force pulling simulation. The MFPT obtained is 1200 ns, a factor of about 3 higher than the MFPT for the final transition of the dynamic path, 11 to G. The long transition time for 1 to G is due to the presence of the two residues Cys468 and Ile591 in the static pathway, which narrow the passage into G substantially. Interestingly, Cys468 is almost next to Leu466, which corresponds to Leu442 in the CODH dimer from *C. hydrogenformans*. The latter was previously described to tighten the channel,[34] similar to what we observe here for CODH/ACS from *M. thermoacetica*. This result is supportive of our observation that CO_2 molecules have a strong preference to diffuse into the active site via a single, dynamically formed path leading from 15 to 11 and across the His113−His116 motif to G.

By combining the results of MD and DFT calculations, we have provided estimates for the rate constants that define the diffusion-reaction model for ligand binding, eq 2. Unfortunately, there are no direct experimental rates available for comparison with the computed CO_2 diffusion rate of $k_{+1} = 4.8 \times 10^3\ s^{-1}\ mM^{-1}$. Kumar et al. determined a rate constant of $2.6 \times 10^4\ s^{-1}\ mM^{-1}$ for the CO driven conversion of C_{red1} into C_{red2} at 300 K (obtained from the experimental value at 5 °C, $4.4 \times 10^3\ s^{-1}\ mM^{-1}$, using an activation energy of 57 kJ/mol).[52] This value provides a lower limit for the diffusion of CO into the active site, and one can expect that the lower limit for CO_2 is somewhat smaller due to its larger size. Further credence to our value in the enzyme is given by the computed Einstein diffusion coefficients for CO_2 in a series of solvents with different polarity, which were in good agreement with experiment (see Table 1).

Interestingly, the DFT calculations on the enzyme active site suggest that chemical bond formation between CO_2 and the Ni atom of the C-cluster ($k_{+2} = 1.3 \times 10^4\ s^{-1}$) occurs on the same time scale as ligand diffusion to the C-cluster, resulting in an overall binding rate constant that is 3−4 orders of magnitude slower than either chemical binding or diffusion alone ($k_{in} = 4.4\ s^{-1}\ mM^{-1}$). Evidently, both steps contribute to the kinetics of ligand binding. This can be easily understood in terms of the steady state formula eq 5. If diffusion out of the protein is much faster than chemical attachment ($k_{-1} \gg k_{+2}$), which is the case here, the overall binding rate (k_{in}) is given by k_{+2} times the equilibrium constant for occupation of the active site cavity ($k_{+1}/k_{-1} = 3 \times 10^{-4}\ mM^{-1}$). Notably, the computed k_{in} is similar to the experimental turnover number of the enzyme ($k_{cat} = 1.3\ s^{-1}$ at 25 °C[50]).

Our results obtained for the CODH dimer are very likely to apply also to the full CODH/ACS tetramer, although a few points need to be discussed in this regard. The main entrance site into the dynamic path, cavity 15, is in the vicinity of the CODH/ACS interface (see Figure 1a) and could potentially become inaccessible to ligands in the ACS bound complex. Our analysis of the binding interface between CODH and ACS in the crystal structure suggests that this is not the case. The three residues at the entrance to cavity 15, Lys178, Gly179, and Glu180, are still accessible to the solvent in the ACS bound complex with an average solvent accessibility of 12.8 Å^2. The presence of the ACS subunit might affect the dynamics of the formation of cavity 15, but it seems unlikely that this will significantly influence the diffusion rate constant, which is governed by the slowest transition from 11 to G. To investigate possible other protein−protein effects, the full ACS/CODH complex needs to be simulated, which is computationally extremely demanding and presently unfeasible for sufficiently long simulation times.

Turning to CO escape, it is remarkable that none of the CO molecules exit the active site via the dynamic pathway. This would invariably lead to diffusion of CO out of the protein and to a loss of two precious reduction equivalents, which is known experimentally not to happen. We find that after CO_2 reduction and formation of the Fe_μ-bound hydroxy ligand (C_{red1} state), the presence of the latter significantly strengthens the local hydrogen-bond network in the active site. The water molecules shown in Figure 5b are rather immobile and exchange with nearby water molecules only very infrequently. The hydrogen-bond network is so robust that it prevents CO from diffusing along the dynamic tunnel into the solvent. The only feasible exit from the active site is to diffuse to cavity 1 and along the static tunnel to the interface where ACS binds. Thus, according to our simulations, it is the change in the hydrogen-bond network in response to reduction of CO_2 to CO that facilitates the directional flow of CO from the C-cluster, where it is produced, to the A-cluster of ACS, where it is utilized.

One may speculate about the benefits of a tetrameric CODH/ACS complex for CO_2 reduction and utilization over a simpler dimeric complex. A key finding in this regard is a cavity close to the D-cluster of CODH (cavity 16 in Figure 1c), halfway between the C- and C′-clusters. This cavity was also found in cavity calculations on the crystal structure, although no Xe was found to bind at this location.[4] We observed a few transitions between 16 and cavities 3A and 3B of the static pathway, implying that the static paths of the two CODH monomer subunits are connected by cavity 16. This could be an important aspect of the working principle of this enzyme. If, for instance, CO cannot bind to the A-cluster of one ACS subunit because it is engaged catalyzing C−C bond formation, the CO molecule could return and diffuse via 3A or 3B to 16 and on to 3A′ or 3B′ to the A′-cluster of the other ACS subunit, which may be ready to bind a CO molecule. Thus, a likely benefit of a tetramer over two dimers is the possibility to synchronize CO formation in CODH and CO consumption in ACS,[53] resulting in a further increase in catalytic efficiency. One should perhaps also mention that the B-cluster of one subunit is much closer to the D- and C-clusters of the other CODH subunit than to those from the same subunit, so that a simpler dimeric CODH/ACS complex is most likely not functional.

5. CONCLUDING REMARKS

In view of current and previous[12,15,18,19,21,27,28] simulations of small ligand diffusion to buried protein active sites, a clearer picture of this fundamental process in chemical biology seems to emerge. Small solvated ligands can readily enter the protein at the surface and move between protein cavities toward the active site through diffusive jumps on the nanosecond time scale. Depending on the size of the molecule, one[27,28] or several[12,15,18] transport channels can be accessed, and they can be either static or dynamically formed. A general feature of the proteins studied is that the transport path(s) merge into a single cavity close to the active site.[12,15,18,19,21,27,28] Typically, the final transit from that cavity into the active site is a bottleneck, which may even become the rate-limiting step for ligand binding depending on the magnitude of the activation free energy for chemical attachment. The last diffusive transition into the active site is typically controlled by the dynamics of a few residues either via steric or electrostatic interactions and has been termed “gating” transition in cases where two or more well-defined states could be discerned (e.g., “open” or “closed”).[14,17] In previous experimental work, it was shown that mutations of two such amino acids at the entrance to the active site of [NiFe]-hydrogenase lead to changes in the inhibitor diffusion rate by several orders of magnitude.[11] The present discovery of a dynamically formed substrate access channel for CODH/ACS suggests that similar effects may occur if two residues at the end of this channel, His113 and His116, are suitably mutated.

■ ASSOCIATED CONTENT

Ⓢ Supporting Information

Details of the molecular models used, protocols for MD simulations and DFT calculations, a table summarizing the calculated kinetic data, two tables summarizing the atomic charges of the C-cluster, and two figures showing MSD and protein RMSD. This material is available free of charge via the Internet at http://pubs.acs.org.

■ AUTHOR INFORMATION

Corresponding Author

j.blumberger@ucl.ac.uk

Notes

The authors declare no competing financial interest.

■ ACKNOWLEDGMENTS

We would like to thank Dr. Christophe Léger for discussions leading to the current work and Prof. Catherine Drennan for discussing with us the setup of the CODH dimer. The simulations were carried out on the UK national high performance computing facility HECToR (University of Edinburgh), to which access was granted via the Materials Chemistry Consortium (EPSRC grant EP/F067496). P.-h.W. acknowledges the Ministry of Education, Republic of China (Taiwan), for a Ph.D. scholarship, and J.B. acknowledges the Royal Society for a University Research Fellowship.

■ REFERENCES

(1) Hyde, C. C.; Ahmed, S. A.; Padlan, E. A.; Miles, E. W.; Davies, D. R. *J. Biol. Chem.* **1988**, *263*, 17857.

(2) Thoden, J. B.; Holden, H. M.; Wesenberg, G.; Raushel, F. M.; Rayment, I. *Biochemistry* **1997**, *36*, 6305.

(3) Montet, Y.; Amara, P.; Volbeda, A.; Vernede, X.; Hatchikian, E. C.; Field, M. J.; Frey, M.; Fontecilla-Camps, J. C. *Nat. Struct. Biol.* **1997**, *4*, 523.

(4) Doukov, T. I.; Iverson, T. M.; Seravalli, J.; Ragsdale, S. W.; Drennan, C. L. *Science* **2002**, *298*, 567.

(5) Darnault, C.; Volbeda, A.; Kim, E. J.; Legrand, P.; VerneÌ€de, X.; Lindahl, P. A.; Fontecilla-Camps, J. C. *Nat. Struct. Mol. Biol.* **2003**, *10*, 271.

(6) Doukov, T. I.; Blasiak, L. C.; Seravalli, J.; Ragsdale, S. W.; Drennan, C. L. *Biochemistry* **2008**, *47*, 3474.

(7) Nienhaus, K.; Palladino, P.; Nienhaus, G. U. *Biochemistry* **2008**, *47*, 935.

(8) Hummer, G.; Schotte, F.; Anfinrud, P. A. *Proc. Natl. Acad. Sci. U.S.A.* **2004**, *101*, 15330.

(9) Armstrong, F. A.; Belsey, N. A.; Cracknell, J. A.; Goldet, G.; Parkin, A.; Reisner, E.; Vincent, K. A.; Wait, A. F. *Chem. Soc. Rev.* **2009**, *38*, 36.

(10) Leroux, F.; Dementin, S.; Burlatt, B.; Cournac, L.; Volbeda, A.; Champ, S.; Martin, L.; Guigliarelli, B.; Bertrand, P.; Fontecilla-Camps, J. C.; Rousset, M.; Leger, C. *Proc. Natl. Acad. Sci. U.S.A.* **2008**, *105*, 11188.

(11) Liebgott, P.-L.; Leroux, F.; Burlat, B.; Dementin, S.; Baffert, C.; Lautier, T.; Fourmond, V.; Ceccaldi, P.; Cavazza, C.; Meynial-Salles, I.; Soucaille, P.; Fontecilla-Camps, J. C.; Guigliarelli, B.; Bertrand, P.; Rousset, M.; Leger, C. *Nat. Chem. Biol.* **2010**, *6*, 63.

(12) Cohen, J.; Kim, K.; Posewitz, M.; Ghirardi, M. L.; Schulten, K.; Seibert, M.; King, P. *Biochem. Soc. Trans.* **2005**, *33*, 80.

(13) Elber, R. *Curr. Opin. Struct. Biol.* **2010**, *20*, 162.

(14) Zhou, H. X.; McCammon, J. A. *Trends Biochem. Sci.* **2010**, *35*, 179.

(15) Wang, P.; Best, R. B.; Blumberger, J. *J. Am. Chem. Soc.* **2011**, *133*, 3548.

(16) Elber, R.; Karplus, M. *J. Am. Chem. Soc.* **1990**, *112*, 9161.

(17) Zhou, H. X.; Wlodek, S. T.; McCammon, J. A. *Proc. Natl. Acad. Sci. U.S.A.* **1998**, *95*, 9280.

(18) Baron, R.; Riley, C.; Chenprakhon, P.; Thotsaporn, K.; Winter, R. T.; Alfieri, A.; Forneris, F.; van Berkel, W. J. H.; Chaiyen, P.; Fraaije, M. W.; Mattevi, A.; McCammon, J. A. *Proc. Natl. Acad. Sci. U.S.A.* **2009**, *106*, 10603.

(19) Baron, R.; McCammon, J. A.; Mattevi, A. *Curr. Opin. Struct. Biol.* **2009**, *19*, 672.

(20) Tan, X.; Loke, H.; Fitch, S.; Lindahl, P. *J. Am. Chem. Soc.* **2005**, *127*, 5833.

(21) Teixeira, V. H.; Baptista, A. M.; Soares, C. M. *Biophys. J.* **2006**, *91*, 2035.

(22) Baltazar, C. S. A.; Teixeira, V. H.; Soares, C. M. *J. Biol. Inorg. Chem.* **2012**, *17*, 543.

(23) Ruscio, J. Z.; Kumar, D.; Shukla, M.; Prisant, M. G.; Murali, T. M.; Onufriev, A. V. *Proc. Natl. Acad. Sci. U.S.A.* **2008**, *105*, 9204.

(24) D’Abramo, M.; Di Nola, A.; Amadei, A. *J. Phys. Chem. B* **2009**, *113*, 16346.

(25) Maragliano, L.; Cottone, G.; Ciccotti, G.; Vanden-Eijnden, E. *J. Am. Chem. Soc.* **2009**, *132*, 1010.

(26) Forti, F.; Boechi, L.; Bikiel, D.; Marti, M. A.; Nardini, M.; Bolognesi, M.; Viappiani, C.; Estrin, D.; Luque, F. J. *J. Phys. Chem. B* **2011**, *115*, 13771.

(27) Wang, P.; Best, R. B.; Blumberger, J. *Phys. Chem. Chem. Phys.* **2011**, *13*, 7708.

(28) Wang, P.; Blumberger, J. *Proc. Natl. Acad. Sci. U.S.A.* **2012**, *109*, 6399.

(29) Lapelosa, M.; Abrams, C. F. *J. Chem. Theory Comput.* **2013**, *9*, 1265.

(30) Ragsdale, S. W.; Pierce, E. *Biochim. Biophys. Acta* **2008**, *1784*, 1873.

(31) Bender, G.; Pierce, E.; Hill, J. A.; Darty, J. E.; Ragsdale, S. W. *Metallomics* **2011**, *3*, 797.

(32) Woolerton, T. W.; Sheard, S.; Pierce, E.; Ragsdale, S. W.; Armstrong, F. A. *Energy Environ. Sci.* **2011**, *4*, 2393.

(33) Sakakura, T.; Choi, J.; Yasuda, H. *Chem. Rev.* **2007**, *107*, 2365.

(34) Dobbek, H.; Svetlitchnyi, V.; Gremer, L.; Huber, R.; Mayer, O. *Science* **2001**, *293*, 1281.

(35) Maynard, E. L.; Lindahl, P. A. *J. Am. Chem. Soc.* **1999**, *121*, 9221.

(36) Seravalli, J.; Ragsdale, S. W. *Biochemistry* **2000**, *39*, 1274.

(37) Daura, X.; Gademann, K.; Jaun, B.; Seebach, D.; van Gunsteren, W.; Mark, A. *Angew. Chem., Int. Ed.* **1999**, *38*, 236.

(38) Buchete, N.; Hummer, G. *J. Phys. Chem. B* **2008**, *112*, 6057.

(39) Dudko, O. K.; Hummer, G.; Szabo, A. *Phys. Rev. Lett.* **2006**, *96*, 108101.

(40) Kung, Y.; Doukov, T. I.; Seravalli, J.; Ragsdale, S. W.; Drennan, C. L. *Biochemistry* **2009**, *48*, 7432.

(41) Scott, W. R. P.; Hünenberger, P. H.; Tironi, I. G.; Mark, A. E.; Billeter, S. R.; Fennen, J.; Torda, A. E.; Huber, T.; Krüger, P.; van Gunsteren, W. F. *J. Phys. Chem. A* **1999**, *103*, 3596.

(42) Berendsen, H. J. C.; Grigera, J. R.; Straatsma, T. P. *J. Phys. Chem.* **1987**, *91*, 6269.

(43) in het Panhuis, M.; Patterson, C.; Lynden-Bell, R. *Mol. Phys.* **1998**, *94*, 963.

(44) Becke, A. D. *Phys. Rev. A* **1988**, *38*, 3098.

(45) Perdew, J. P. *Phys. Rev. B* **1986**, *33*, 8822.

(46) Jeoung, J.-H.; Dobbek, H. *Science* **2007**, *318*, 1461.

(47) Amara, P.; Mouesca, J.-M.; Volbeda, A.; Fontecilla-Camps, J. C. *Inorg. Chem.* **2011**, *50*, 1868.

(48) Gu, W. W.; Seravalli, J.; Ragsdale, S. W.; Cramer, S. P. *Biochemistry* **2004**, *43*, 9029.

(49) Ralston, C. Y.; Wang, H. X.; Ragsdale, S. W.; Kumar, M.; Spangler, N. J.; Ludden, P. W.; Gu, W.; Jones, R. M.; Patil, D. S.; Cramer, S. P. *J. Am. Chem. Soc.* **2000**, *122*, 10553.

(50) Kumar, M.; Lu, W.-P.; Ragsdale, S. W. *Biochemistry* **1994**, *33*, 9769−9777.

(51) Volbeda, A.; Fontecilla-Camps, J. *J. Biol. Inorg. Chem.* **2004**, *9*, 525.

(52) Kumar, M.; Lu, W. P.; Liu, L.; Ragsdale, S. W. *J. Am. Chem. Soc.* **1993**, *115*, 11646.

(53) Maynard, E. L.; Lindahl, P. A. *Biochemistry* **2001**, *40*, 13262.

(54) Jähne, B.; Heinz, G.; Dietrich, W. *J. Geophys. Res.* **1987**, *92*, 10767.

(55) Frank, M. J. W.; Kuipers, J. A. M.; van Swaaij, W. P. M. *J. Chem. Eng. Data* **1996**, *41*, 297.

(56) Akgerman, A.; Gainer, J. *J. Chem. Eng. Data* **1972**, *17*, 372.